Computational study of geothermal thermoelectric generators with phase change heat exchangers

Leyre Catalan[a,*], Miguel Araiz[a], Patricia Aranguren[a], David Astrain[a]

[a]*Department of Engineering, Institute of Smart Cities, Public University of Navarre, Pamplona, Spain*

Abstract

The use of thermoelectric generators with phase change heat exchangers has demonstrated to be an interesting and environmentally friendly alternative to enhanced geothermal systems (EGS) in shallow hot dry rock fields (HDR), since rock fracture is avoided. The present paper studies the possibilities of the former proposal in a real location: Timanfaya National Park (Canary Islands, Spain), one of the greatest shallow HDR fields in the world, with 5000 m^2 of characterized geothermal anomalies presenting temperatures up to 500 °C at only 2 m deep. For this purpose, a computational model based on the thermal-electrical analogy has been developed and validated thanks to a real prototype, leading to a relative error of less than 8 %. Based on this model, two prototypes have been designed and studied for two different areas within the park, varying the size of the heat exchangers and the number of thermoelectric modules installed. As a result, the potential of the solution is demonstrated, leading to an annual electricity generation of 681.53 MWh thanks to the scalability of thermoelectric generators. This generation is obtained without moving parts nor auxiliary consumption, thus increasing the robustness of the device and removing maintenance requirements.

Keywords:
Computational model; Thermoelectric generator; Geothermal; Hot Dry Rock; Phase change; Timanfaya

---

1. Introduction

In the last decade, there has been much progress in the use of renewable energies and energy efficiency measures [1–3]. Nevertheless, the international climate goals established under the Paris Agreement are not on track to be met [4]. Therefore, there still exists a necessity for further development of renewable energies.

Among all the renewable sources, geothermal energy stands out because it is not affected by weather, it is stable, it can provide both heat and electricity, it has a high capacity factor, it can be used as base-load power, and it has a high thermal efficiency. However, despite these advantages, geothermal energy is positioned behind other renewable energies, especially in electricity generation, with only 13.3 GW installed accounting for less than 0.4 % of global electricity production [5].

Recently, in order to increase the growth rate of geothermal power, thermoelectric generators (TEGs) have been proposed as an alternative to traditional cycles [6]. TEGs are devices formed by the interconnection of one or multiple thermoelectric modules (TEMs) that, due to Seebeck effect, generate electricity based on the heat received from a hot source, emitting the rest to a cold sink, which is normally the environment. Carnot theorem applied to a TEG concludes that the efficiency of the system increases as the sides of the TEMs approach the temperature of the heat source and sink. Therefore, the introduction of heat exchangers between the modules and each of the thermal reservoirs becomes necessary in order to maximize the temperature difference. In fact, Astrain et al. demonstrated that an improvement of 10 % in the thermal resistance of the heat exchangers leads to an 8 % higher generation [7]. Fin dissipators, heat exchangers with a fluid as heat carrier, and heat exchangers based on phase change are the most common alternatives found in TEGs [8].

Most of the proposed geothermal thermoelectric generators (GTEGs) use heat exchangers with a fluid as heat carrier, similarly to conventional geothermal cycles. Thus, a fluid is pumped into the ground so that it absorbs geothermal heat. The heat is then released to the thermoelectric modules, which transform part of it into electricity, releasing the rest into the environment by means of another heat exchanger based on a fluid, analogously to condensers. Since one of the main drawbacks of thermoelectricity is its low efficiency, these GTEGs are designed for low temperature geothermal fields ($T < 150$ °C), where they can become competitive in comparison to binary cycles (ORC and Kalina), the most commonly used technology in the low temperature range.

Among low temperature GTEGs with heat exchangers with a fluid as heat carrier, their integration downhole in oil and gas wells seems to have the highest potential. Thanks to this synergy, Wang et al. estimated

---

[*] Corresponding author

Nomenclature

Variables

α	Seebeck coefficient (K/W)
ΔP_{sat}	Difference in saturation pressure corresponding to ΔT_{sat} (Pa)
ΔT_{sat}	Difference between wall and saturation temperature (°C)
$\dot{Q}$	Heat flux (W)
ϵ	Ratio between equivalent radius, e.g. for the hot side $\epsilon = \sqrt{A_{TEM}/\pi}/\sqrt{A_c/\pi}$
η	Efficiency
γ	Surface tension (N/m)
λ_c	$\lambda_c = \pi + 1/(\sqrt{\pi} \cdot \epsilon)$
μ	Dynamic viscosity (Pa · s)
ν	Kinematic viscosity (m^2/s)
ϕ_c	Parameter given by Equation 13
ψ	Dimensionless constriction resistance
ρ	Electrical resistivity ($\Omega \cdot$ m)
σ	Thomson coefficient (V/K)
τ	$\tau = e_c/\sqrt{A_c/\pi}$
A	Area (m^2)
Bi	Biot number $Bi = h_b \cdot (\sqrt{A_c}/\pi)/k$
cp	Specific heat (J/kg · K)
D	Diameter (m)
d	Density (kg/m^3)
e	Thickness (m)
Et	Electromotive force (V)
G	Total mass flux (liquid + area) per unit of area
g	Gravity acceleration (m/s^2)
h	Heat transfer coefficient (W/m^2 · K)
I	Intensity (A)
i_{lg}	Latent heat of vaporization (J/kg)
J_g	Dimensionless vapour velocity
k	Thermal conductivity (W/m · K)
L	Length (m)
L_{ch-fin}	Characteristic length of a fin $L_{ch-fin} = L_{fin} + (t/2)$
L_{ch}	Characteristic length (m)
m_w	$m_w = \sqrt{h_w \cdot S_w^2/(k_w \cdot D_w)}$
m_{fin}	$m_{fin} = \sqrt{2 \cdot h_{conv}^H/k \cdot t}$
N	Number
Nu	Nusselt number $Nu = h \cdot L_{ch}/k$
P	Electric power (W)
p_r	Reduced pressure
Pr	Prandtl number $Pr = cp \cdot \mu/k$
R	Thermal resistance (K/W)
R_0	Internal electrical resistance (Ω)
R_{load}	Load electrical resistance (Ω)
Re	Reynolds number $Re = v \cdot L_{ch}/\nu$
S	Space between (m)
t	Fin thickness (m)
V	Voltage (V)
v	Velocity (m/s)
x	Vapour quality
y	Mass fraction
Z	Shah's correlating parameter: $Z = (1/x - 1^{0.8} p_r^{0.4})$

Subscripts and Superscripts

air	Air / Wind
amb	Ambient
b	Boiling
C	Cold side
c	Condensation / Condenser
co	Contact
$cond$	Pure conduction
$const$	Constriction
$conv$	Convective
e	External
ev	Evaporator
exp	Experimental
fin	Fin
G	Geothermal gases
g	Gas
H	Hot side
i	Internal
ins	Insulator
k	Conductive
l	Liquid
n	Semiconductor n
p	Semiconductor p
R	Rope heaters
s	Surface
sat	Saturation
sim	Simulated
sup	Per unit of area
T	Temperature (°C)
t	Tubes
tc	Thermocouple
u	Union material
w	Wired fins
i	Node number

Abbreviations

CHE	Cold side Heat Exchanger
EGS	Enhanced Geothermal System
FD	Fin dissipator
GTEG	Geothermal Thermoelectric Generator
HDR	Hot Dry Rock
HHE	Hot side Heat Exchanger
LT	Loop Thermosyphon
ORC	Organic Rankine Cycle
TEG	Thermoelectric Generator
TEM	Thermoelectric Module
TPCT	Two Phase Closed Thermosyphon

that 8538 W can be produced in a vertical well located in China, where there exists a 100 °C temperature difference [9], and 128 024 W in a horizontal one, also in China, with a 156 °C gradient [10]. Apart from the combination of geothermal energy and hydrocarbons, there also exist some proposals of GTEGs for traditional low temperature geothermal systems with again heat exchangers with a fluid as heat carrier. Suter et al. modeled and optimized a 1 kW GTEG working with a 100 °C gradient by modifying different operating parameters and geometries [11, 12]. Liu et al. also designed a 1 kW GTEG consisting of 600 TEMs and working with a temperature difference of 120 °C [13]. In order to obtain this design, they had previously built a real prototype with 96 TEMs that generated 160 W under a 120 °C gradient, and by extrapolation, 500 W with a temperature difference of 200 °C [14, 15]. Niu et al. as well as Ahiska and Mamur also built a prototype in order to demonstrate the viability of the technology. Thus, Niu et al. generated 146.5 W with 56 TEMs and 120 °C gradient [16], and Ahiska and Mamur, on their behalf, produced 41.6 W with 20 TEMs and a temperature difference of 67 °C [17, 18].

Only a couple of examples of GTEGs for high temperature geothermal fields can be found in the literature. On the one hand, Banerjee studied the installation of TEGs in offshore wind turbine monopiles to extract geothermal energy and produce up to 242 kW using again heat exchangers with a fluid as heat carrier [19]. On the other hand, Catalan et al. proposed the use of GTEGs in shallow hot dry rock (HDR) fields [20], one of the most extended and potential geothermal fields [21], leading to a generation of up to 3.2 W per module with a temperature difference between sources of 180 °C. The novelty of this proposal was not only the application itself, but also their conclusion, experimentally demonstrating that passive heat exchangers based on phase change are the most suitable ones for both sides of GTEGs, with a 54% higher generation than fin dissipators.

Heat exchangers based on phase change take advantage of the latent heat of an internal fluid, which is cyclically vaporizing and condensing, to transfer a large quantity of heat over relatively long distances, thus leading to a low thermal resistance. In combination with thermoelectric generators, their use has generalized in the last years and these heat exchangers can be found in several applications: waste heat recovery from industries [22, 23], automotive thermoelectric generators [24–26], or concentrated solar thermoelectric generators [27] among others. Some of them include an auxiliary consumption to reduce even more the thermal resistance of the heat exchangers, especially improving convection with the environment with the aid of a ventilator, while others do not include any auxiliary component, obtaining a completely passive heat exchanger.

In GTEGs, there do not exist many examples with phase change heat exchangers. Huang et al. developed a thermoelectric micro-generator with a heat pipe as hot side heat exchanger and fin dissipators as cold side ones, to power forest wireless sensors in remote areas using the temperature difference between the soil and the air [28, 29]. On their behalf, Dell et al. combined conventional geothermal steam pipes with a thermoelectric generator with heat pipes as cold side heat exchangers, so that different electronics systems were powered [30, 31]. Catalan et al. were the first ones proposing a GTEG with passive phase change heat exchangers at both sides of the thermoelectric modules for high scale generation, leading to a robust generator with minimal maintenance requirements. In their application to HDR fields, their use also prevents rock fracture and induced seismicity, one of the most critical issues of enhanced geothermal systems (EGS), the only existing technique nowadays.

The present paper delves into the study of these GTEGs with passive phase change heat exchangers for high temperature HDR fields. More specifically, its objective is to analyze the influence of different parameters taking as reference a real HDR field, Timanfaya National Park (Canary Islands, Spain), whose potential will be also estimated. In order to achieve this objective, it will be necessary to develop and experimentally validate a computational model. Section 2 details the operation of a GTEG with phase change heat exchangers, Section 3 describes the computational model that has been developed. This computational model has been validated with experimental results, as described in Section 4. Based on it, Section 5 describes the analysis of different parameters and the potential of the proposed solution considering as reference the HDR field located at Timanfaya National Park (Canary Islands, Spain). Finally, Section 6 summarizes the main conclusions obtained in the present paper.

2. GTEG with phase change heat exchangers

In order to leverage shallow hot dry rock (HDR) fields, Catalan et al. demonstrated the feasibility of thermoelectric generators as a greener alternative to enhanced geothermal systems (EGS) [20]. In their study of different heat exchangers, they concluded that those based on phase change are the most adequate ones for GTEGs. Hence, since the present paper delves into their development, analyzing the influence of different parameters and the potential of their large scale implementation in a real location by means of a computational model, this section details the operation of the GTEG that will be modeled, including not only the generator itself but also the heat source.

HDR fields represent the heat source of the generator. These fields can be defined as geothermal fields characterized by high temperature compact rocks, where the absence of both reservoir and fluid that acts as a heat carrier prevents the existence of a geothermal system, which is necessary for traditional geothermal power generation. The present paper focuses on shallow HDR fields, where

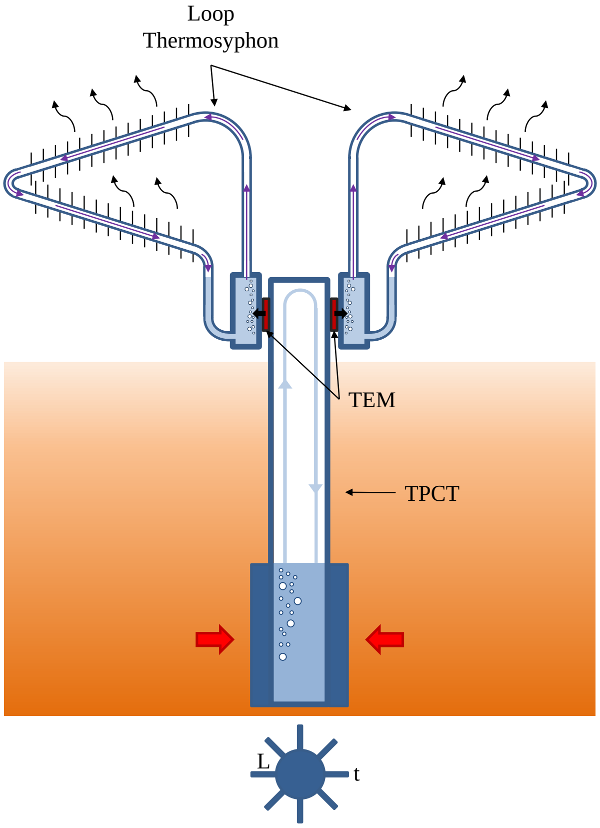

Figure 1: Schematics of the operation of a cylindrical geothermal thermoelectric generator (GTEG) with phase change heat exchangers.

it would be easy to drill a borehole to insert the generator. Due to the absence of a fluid as heat carrier and the low diffusivity of the rocks, the transmission of heat to the GTEG occurs by convection with the air that is naturally heated up by the rocks [32]. Although this may seem an insufficient heat source, in the HDR taken as reference in this paper and that is more deeply described in Section 5, natural gas flows ascending at velocities of up to 11.15 m/s have been measured at temperatures higher than 200 °C, so it definitely is a heat source to consider.

Figure 1 depicts the schematics of the operation of a cylindrical GTEG with phase change heat exchangers installed in a HDR field. The hot side heat exchanger is a two phase closed thermosyphon (TPCT), i.e. a hermetically sealed container filled with a small amount of working fluid [33]. In contact with the hot air, the internal fluid vaporizes and, due to natural convection, ascends to the upper part of the container, where it condensates releasing heat to the TEMs. Since this process is driven by phase change, heat is absorbed and transported with a minimal temperature difference regardless of the distance, as it has been previously demonstrated with a 400 m long TPCT [34]. In order to improve the convection between the hot air and the TPCT, the present paper will consider the addition of vertical fins to the external part of this hot side heat exchanger.

The heat released in the condensation of the TPCT is transmitted to the thermoelectric modules (TEMs), located overground in the upper part of that heat exchanger. These TEMs transform part of the received heat into electricity, releasing the rest to the cold side heat exchangers. In this paper, commercial bismuth telluride TEMs will be considered.

The heat released by the TEMs needs to be dissipated into the environment. Heat exchangers based on phase change have been demonstrated to be the most appropriate ones for this purpose for medium temperature range under 300 °C [35] and the considered application of GTEGs [20]. Thus, loop thermosyphons will be considered in this paper due to their compactness. An individual loop thermosyphon will be used per each TEM.

Thanks to the use of heat exchangers based on phase change at both side of the TEMs, the proposed solution of GTEG presents several advantages: it is robust, modular, noiseless, independent of the depth of the borehole, has a minimal environmental impact, and does not present moving parts, removing maintenance requirements, nor auxiliary equipment, thus maximizing power generation.

3. Computational Model

In order to study the feasibility of GTEGs, most of the existing proposals use computational models. The use of these models has spread in the last years becoming an indispensable tool for the design, analysis, and optimization of real applications, reducing the necessity of building prototypes and limiting the number of experimental tests necessary in order to obtain significant information, which translates in cost savings. In the case of GTEGs, these aspects gain even more importance due to the high scale implied. Aligned with the objective of the present paper, this section describes the computational model developed for the analysis of GTEGs with phase change heat exchangers at both sides of the TEMs.

In the modeling of TEGs, there exist four major kinds of models: standard simplified models, analytical models, models based on the electrical analogy between heat transfer and electricity, and numerical models based on finite elements [36]. The models used for GTEGs are mainly simplified models, which neglect Thomson effect and assume constant thermoelectric properties. Most of them, concentrate on a correct simulation of the heat exchangers, but simplify the modeling of the TEMs, leading to a slight deviation in the calculation of power generation [36].

Models based on the electrical analogy between heat transfer and electricity have demonstrated to be accurate alternatives with an assumable computational cost in different applications [23, 36–38]. This thermal-electrical analogy also permits modeling heat exchangers based on phase change, as Araiz et al. demonstrated for a loop thermosyphon with errors lower than 9% [39]. Based on this

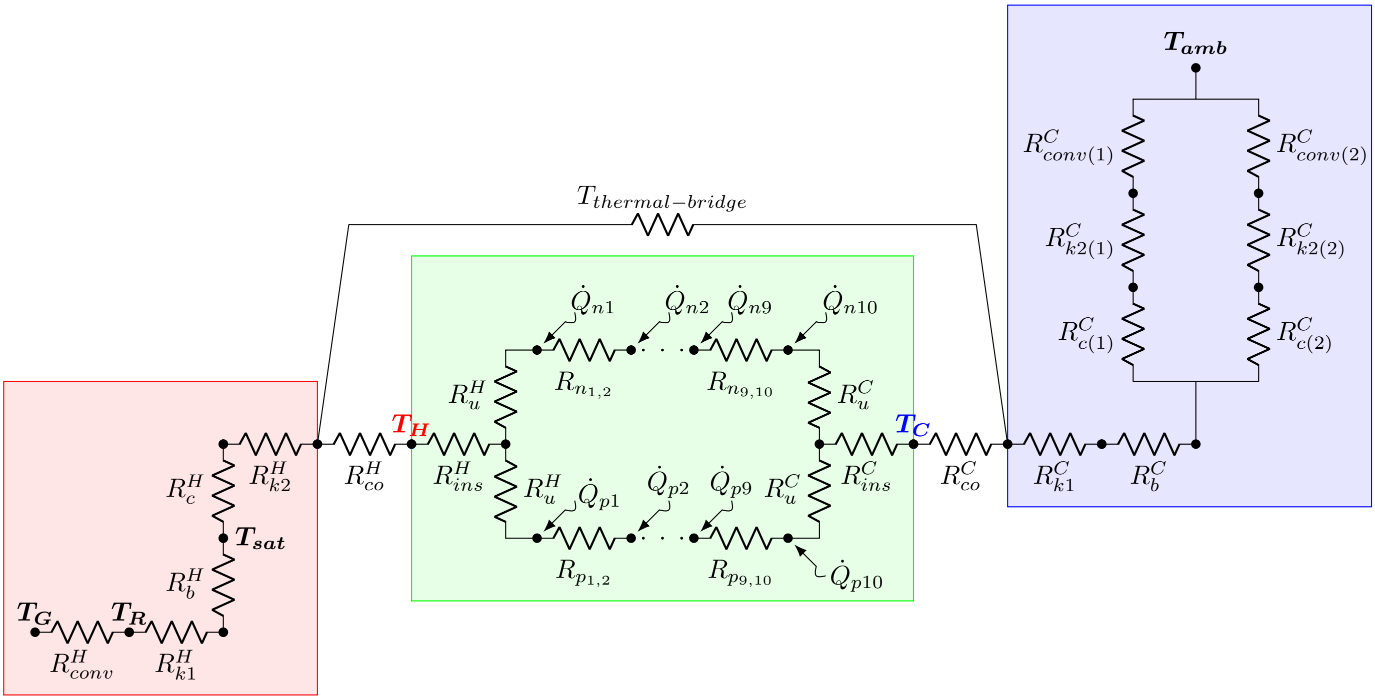

Figure 2: Thermal-electrical analogy of a GTEG with phase change heat exchangers.

characterization, they subsequently developed a computational model of a complete TEG with loop thermosyphons as cold side heat exchangers, and fin dissipators as hot side ones [40]. Other authors, such as Brito et al. and Pacheco et al. also use the electrical analogy in order to model heat exchangers based on phase change [25, 41, 42]. In particular, they model TEGs with heat pipes in the hot side and heat exchangers based on a fluid in the cold one in order to generate electricity from the exhaust gases of vehicles, although the resolution of the TEMs is simplified, neglecting Thomson effect and variable thermoelectric properties.

The computational model developed in this paper also follows the electrical analogy between heat transfer and electricity, and it considers, for the first time, heat exchangers based on phase change at both sides of the TEMs. The thermal-electrical analogy is actually derived from the application of the implicit finite difference method to heat conduction equation. Its basic idea consists in discretizing the system in several nodes. The solution of the original problem is obtained for those finite number of nodes.

Figure 2 depicts the discretization of a general GTEG, such as the one described in Section 2. For simplicity, the explanation of the system will be performed according to the three different blocks that compose it: hot side heat exchanger (red block), TEMs (green block) and cold side heat exchanger (blue block). Afterward, it will be described the union between these several blocks, which considers contact thermal resistances, as well as other phenomena such as thermal bridges. In their modeling, some simplification hypothesis have been considered: (i) all materials are homogeneous, with uniform composition and structure; (ii) the insulation of the electric circuit is perfect and the electric current is unidimensional; (iii) the heat flux is also unidimensional, thus lateral heat losses are neglected; (iv) only the stationary regime is considered; and (v) no subcooling nor reheating occur in the heat exchangers. Finally, once all the thermal resistances have been described, the resolution methodology to solve the system and obtain the temperature of each node is detailed.

3.1. Hot Side Heat Exchanger

The hot side heat exchanger is a two phase closed thermosyphon (TPCT). As a result of its discretization, the red block of Figure 2 shows the thermal-electrical analogy taking into account all the phenomena occurring in this phase change heat exchanger. Superscript H refers to the hot side heat exchanger.

Following the heat flux from the air heated up by the geothermal HDR field, the first thermal resistance represents the convection between the hot air and the TPCT, which have fins in order to improve the heat transfer. This resistance can be estimated as follows:

$$R^H_{conv} = \frac{1}{h^H_{conv} \cdot A^H_{conv} \cdot \eta^H_{fin}} \tag{1}$$

where h^H_{conv} is the convective heat transfer coefficient derived from the Nusselt expression deduced by Sieder and Tate's correlation for forced convection in pipes (Equation 2) that is valid for Prandtl and Reynolds numbers in the ranges $[0.7, 160]$ and $\left[10^4, 10^6\right]$ respectively [43], A^H_{conv} is the area in contact with the hot air (taking into account the fins and up to the interior fluid's height), and

η_{fin} is the efficiency of the fins, which is estimated with Equation 3 [44].

$$Nu = 0.027 \cdot Re^{0.8} \cdot Pr^{1/3} \cdot \left(\frac{\mu}{\mu_s}\right)^{0.14} \tag{2}$$

$$\eta_{fin} = 1 - \frac{N_{fin} \cdot A_{fin}}{A^H_{conv}} \left(1 - \frac{\tanh(m_{fin} \cdot L_{ch-fin})}{m_{fin} \cdot L_{ch-fin}}\right) \tag{3}$$

The next thermal resistance R^H_{k1} represents the heat conduction through the wall of the evaporator, which is considered to take up to the internal fluid's height. In case of having a cylindrical TPCT, this resistance is estimated according to Equation 4, while for a TPCT with planar surfaces, Equation 5 applies [43].

$$R^H_{k1} = \frac{\ln\left(D^H_e / D^H_i\right)}{2 \cdot \pi \cdot L \cdot k} \tag{4}$$

$$R^H_{k1} = \frac{e^H}{k^H \cdot A^H_{k1}} \tag{5}$$

The heat conducted through the wall causes the vaporization of part of the internal working fluid contained inside the TPCT. This process is modeled by the boiling thermal resistance R^H_b, for which a boiling coefficient is necessary (Equation 6). Assuming that nucleate pool boiling is taking place, the correlation proposed by Forster and Zuber in 1955 is used (Equation 7) [45]. This expression is commonly used due to its simplicity, although it does not take into account the combination between the surface and the boiling fluid [46].

$$R^H_b = \frac{1}{h^H_b \cdot A^H_b} \tag{6}$$

$$h^H_b = \frac{0.00122\ \Delta T_{sat}^{\ 0.24}\ \Delta P_{sat}^{\ 0.75}\ cp_l^{\ 0.45}\ d_l^{\ 0.49}\ k_l^{\ 0.79}}{\gamma^{\ 0.5}\ i_{lg}^{\ 0.24}\ \mu_l^{\ 0.29}\ d_g^{\ 0.24}} \tag{7}$$

Next, the vapor ascends, due to its lower density, to the upper part of the TPCT, where it condensates. In order to calculate the condensation thermal resistance, it is necessary to consider the area of condensation of all the TEMs, and a condensation coefficient (Equation 8). The phenomenon that takes place in this case is film condensation on a vertical plate. Therefore, the heat transfer coefficient is determined by Equation 9 [46], which neglects convection effects in the film and assumes a constant wall temperature.

$$R^H_c = \frac{1}{h^H_c \cdot A^H_c} \tag{8}$$

$$h^H_c = 0.943 \left[\frac{k_l^3\ d_l\ (d_l - d_g)\ g\ i_{lg}}{\mu_l\ \Delta T_{sat}\ L_c}\right]^{\frac{1}{4}} \tag{9}$$

Lastly, the thermal resistance R^H_{k2} represents the last element of the electrical analogy of a TPCT and deals with two different phenomena. On the one hand, it considers the conduction that takes place in the condenser. In this case, and since the TEMs need to be in contact with the upper part of the TPCT, only the expression of heat conduction for planar surfaces is considered (Equation 10) [43]. In this equation, subscript c has been added to differentiate that it refers to the condenser part of the TPCT.

$$R^H_{k2,cond} = \frac{e^H_c}{k^H \cdot A^H_c} \tag{10}$$

On the other hand, due to the fact that condensation occurs in an area a bit bigger than that of the module, constriction effect appears causing an increase in the thermal resistance. Lee et. al [47] estimated that constriction resistance can be calculated as:

$$R^H_{k2,const} = \frac{\Psi^H}{N_{TEM} \cdot k^H \cdot \sqrt{A_{TEM}}} \tag{11}$$

where N_{TEM} is the number of TEMs, k^H is the thermal conductivity of the material, A_{TEM} the area of a thermoelectric module, and Ψ^H is the dimensionless constriction resistance expressed by Equation 12.

$$\Psi^H = \frac{1}{2} \cdot (1 - \epsilon^H)^{3/2} \cdot \Phi^H_c \tag{12}$$

in which ϵ^H is the ratio between the equivalent radius of a module and the equivalent radius of the region in which condensation occurs per each module and Φ^H_c follows Equation 13.

$$\Phi^H_c = \frac{\tanh(\lambda^H_c \cdot \tau^H) + \frac{\lambda^H_c}{Bi^H}}{1 + \frac{\lambda^H_c}{Bi^H} \cdot \tanh(\lambda^H_c \cdot \tau^H)} \tag{13}$$

Thus, the thermal resistance R^H_{k2} is finally calculated by simply adding the conduction and constriction resistances:

$$R^H_{k2} = R^H_{k2,cond} + R^H_{k2,const} \tag{14}$$

3.2. Thermoelectric Modules

The second block, corresponding to the TEMs and depicted in green color in Figure 2, is the element most difficult to model since phenomena related to heat transmission and thermoelectricity take part at the same time. A TEM is made up of several thermocouples connected electrically in series and thermally in parallel. Each thermocouple itself is composed of an n-type semiconductor united by means of a conductive material to a p-type semiconductor.

In order to capture all the phenomena that occur simultaneously in a TEM, in each thermocouple, each semiconductor has been discretized into 10 nodes since this leads to accurate results without increasing the computational cost [23, 37, 38], and temperature dependent properties have been considered. Since the dominant heat transfer mechanism is conduction, all the thermal resistances of semiconductors n and p are calculated by means of Equation 15 and Equation 16 respectively, in which it has been considered that the N_{tc} thermocouples that make up a TEM are connected thermally in parallel, similarly to the N_{TEM} thermoelectric modules.

$$R_{n(i,i+1)} = \frac{L_n/9}{N_{TEM} \cdot N_{tc} \cdot k_{n(i,i+1)} \cdot A_n} \qquad i = 1-9 \tag{15}$$

$$R_{p(i,i+1)} = \frac{L_p/9}{N_{TEM} \cdot N_{tc} \cdot k_{p(i,i+1)} \cdot A_p} \qquad i = 1-9 \tag{16}$$

In these equations, L_n and L_p are the lengths of the semiconductors, $k_{n(i,i+1)}$ and $k_{p(i,i+1)}$ are their thermal conductivities calculated at the mean temperature of their delimiting nodes i and $i+1$, and A_n and A_p are their cross-sectional areas.

Both semiconductors are united by a conductive material. Many times, the thermal resistance of this union material is neglected due to its high thermal conductivity in comparison to the semiconductors. However, in order to duly resemble the model to reality, the present paper considers it. As shown in Equation 17, half of this material is considered in the n branch and the other half in the p one.

$$R_u^H = R_u^C = \frac{L_u}{N_{TEM} \cdot N_{tc} \cdot k_u \cdot A_u/2} \tag{17}$$

The last thermal resistances that need to be considered in the model are those corresponding to the electrical insulating material that protects the internal circuit and provides firmness to each TEM.

$$R_{ins}^H = R_{ins}^C = \frac{L_{ins}}{N_{TEM} \cdot k_{ins} \cdot A_{ins}} \tag{18}$$

Apart from the former thermal resistances, it is necessary to consider heat fluxes in the semiconductor nodes in order to model the thermoelectric effects that take place. All nodes generate heat due to Joule and Thomson effect. Furthermore, in extreme nodes, heat is also produced by Peltier effect in the semiconductors and Joule effect in the electrical contacts. For simplicity, only the expressions corresponding to n semiconductor are shown.

$$\begin{split}\dot{Q}_{n1} = N_{TEM} \cdot N_{tc} \cdot \Bigg[\frac{-(\alpha_{p1} - \alpha_{n1}) T_{n1}}{2} I + \frac{\rho_{u,n}^{sup}}{A_n} I^2 \\ + \rho_{n1} \cdot I^2 \frac{L_n/18}{A_n} - \sigma_{n1} \cdot I \frac{T_{n1} - T_{n2}}{2} \Bigg]\end{split} \tag{19}$$

$$\begin{split}\dot{Q}_{n(i)} = N_{TEM} \cdot N_{tc} \cdot \Bigg(\rho_{n(i)} \cdot I^2 \frac{L_n/9}{A_n} \\ - \sigma_{n(i)} \cdot I \frac{T_{n(i-1)} - T_{n(i+1)}}{2} \Bigg) \qquad i = 2-9\end{split} \tag{20}$$

$$\begin{split}\dot{Q}_{n,10} = N_{TEM} \cdot N_{tc} \cdot \Bigg[\frac{-(\alpha_{p10} - \alpha_{n10}) T_{n10}}{2} I + \frac{\rho_{u,n}^{sup}}{A_n} I^2 \\ + \rho_{n10} \cdot I^2 \frac{L_n/18}{A_n} - \sigma_{n10} \cdot I \frac{T_{n9} - T_{n10}}{2} \Bigg]\end{split} \tag{21}$$

Seebeck effect is considered in the calculation of the power generated. Considering an electrical resistance R_{load} connected to the system, the power generated in this resistance can be calculated according to Equation 22.

$$P = N_{TEM} \cdot Et^2 \frac{m}{R_0 \cdot (m+1)^2} \tag{22}$$

where Et is the electromotive force generated per TEM (Equation 23), R_0 is the internal resistance of each TEM (Equation 24), and m is a parameter calculated with Equation 25 in case that the TEMs are connected in series or with Equation 26 in case of a parallel connection.

$$\begin{split}Et = N_{tc} \cdot \Bigg[\alpha_{p1} T_{p1} - \alpha_{n1} T_{n1} - \alpha_{p10} T_{p10} + \alpha_{n10} T_{n10} \\ - \sigma_{p1} \frac{T_{p1} - T_{p2}}{2} + \sigma_{n1} \frac{T_{n1} - T_{n2}}{2} - \sigma_{p10} \frac{T_{p9} - T_{p10}}{2} \\ + \sigma_{n10} \frac{T_{n9} - T_{n10}}{2} - \sum_{i=2}^{9} \left(\sigma_{p(i)} \frac{T_{p(i-1)} - T_p(i+1)}{2} \right) \\ + \sum_{i=2}^{9} \left(\sigma_{n(i)} \frac{T_{n(i-1)} - T_{n(i+1)}}{2} \right) \Bigg]\end{split} \tag{23}$$

$$\begin{split}R_0 = N_{tc} \cdot \Bigg[\frac{L_p/9}{A_p} \left(\frac{\rho_{p1}}{2} + \frac{\rho_{p,n_p}}{2} + \sum_{i=2}^{n_p} \rho_{p(i)} \right) \\ + 2 \frac{\rho_{u,p}^{sup}}{A_p} + \frac{L_n/9}{A_n} \left(\frac{\rho_{n1}}{2} + \frac{\rho_{p,n_n}}{2} + \sum_{i=2}^{n_n} \rho_{n(i)} \right) \\ + 2 \frac{\rho_{u,n}^{sup}}{A_n} \Bigg]\end{split} \tag{24}$$

$$m^{series} = \frac{R_{load}}{N_{TEM} \cdot R_0} \tag{25}$$

$$m^{parallel} = \frac{N_{TEM} \cdot R_{load}}{R_0} \tag{26}$$

3.3. Cold Side Heat Exchanger

Similarly to the hot side heat exchanger, the cold side one is also a biphasic thermosyphon. Nonetheless, its geometry changes, being a loop thermosyphon in this case, with a common evaporator and two sets of tubes for releasing the heat to the environment. As a consequence, some of the expressions change and two branches need to be considered.

Blue block in Figure 2 depicts the discretization of this cold side heat exchanger, composed of five different thermal resistances, and where superscript C refers to the cold side. Following again the direction of the heat flux, the first thermal resistance that characterizes the cold loop thermosyphon $R^C_{k,1}$ represents the addition of two phenomena: conduction through the wall of the evaporator and spreading. Hence, the former resistance is modeled again according to Fourier law (Equation 5). Apart from pure conduction, $R_{k,1}$ also takes into account the spreading phenomenon, which occurs because heat flows from a small surface of the size of a TEM to a larger one, the evaporator's base. This thermal resistance is calculated as the constriction one (Equation 11), but considering the evaporator's area instead of the condenser one.

After conduction and spreading, heat causes the vaporization of the internal working fluid. In order to calculate this boiling resistance, Forster and Zuber's correlation is again used (Equation 6). Nonetheless, in this case, it has been considered a mixture of two substances as working fluid. The properties of the mixture are obtained with REFPROP [48], except the thermal conductivity, kinematic and dynamic viscosities, which have been calculated with Filippov and Novoselova [49], Gambill [50] and Graham's [51] models respectively (Equation 27, 28, 29) using the REFPROP properties of each substance.

$$k = k_1 \cdot y_1 + k_2 \cdot y_2 - 0.72 \mid k_1 - k_2 \mid y_1 \cdot y_2 \tag{27}$$

$$\nu^{1/3} = y_1 \cdot \nu_1^{1/3} + y_2 \cdot \nu_2^{1/3} \tag{28}$$

$$\mu = y_1 \cdot \mu_1 + y_2 \cdot \mu_2 \tag{29}$$

Next, the vaporized fluid condensates. Nevertheless, in the case of a loop thermosyphon, this process occurs along the loop tubes rather than on a vertical plate as it happens in the hot TPCT. Hence, the heat transfer coefficient of Equation 8 varies. According to Shah's correlation [52], this coefficient depends on the regime of vapor calculated with the dimensionless vapour velocity J_g (Equation 30).

$$J_g = \frac{x \cdot G}{(g \cdot D_{in} \cdot d_g \cdot (d_l - d_g))^{0.5}} \tag{30}$$

If $J_g \geq 1/(2.4 \cdot Z + 0.73)$ (with $Z = (1/x - 1^{0.8} p_r^{0.4})$), $h_c = h_I$, else if $J_g \leq 0.89 - 0.93 \cdot exp(-0.087 \cdot Z^{-1.17})$, $h_c = h_{Nu}$, else $h_c = h_I + h_{Nu}$, where

$$\begin{aligned} h_I = 0.023 \cdot Re^{0.8} \cdot Pr^{0.4} \cdot \left(\frac{\mu_l}{14 \cdot \mu_g}\right)^{0.0058+0.557p_r} \\ \cdot \left[(1-x)^{0.8} + \frac{3.8 \cdot x^{0.76}(1-x)^{0.04}}{p_r^{0.38}}\right] \end{aligned} \tag{31}$$

$$h_{Nu} = 1.32 \cdot Re^{-1/3} \left[\frac{d_l \cdot (d_l - d_g) \cdot g \cdot k_l^3}{\mu_l^2}\right]^{1/3} \tag{32}$$

The former correlation has shown to be in good agreement with 22 different fluids; horizontal, vertical, and downward-inclined tubes; tube diameters from 2 to 49 mm; reduced pressures from 0.0008 to 0.9; flow rates from 4 to 820 kg/m^2·s; all liquid Reynolds numbers from 68 to 85 000; and all liquid Prandtl numbers from 1 to 18 [52].

After condensation, conduction needs to be considered. Due to the circular shape of the tubes, in this case, according to Fourier law, Equation 4 applies again. Nonetheless, it is important to note that the length of all the loops must be considered.

Finally, convection with the environment needs to be taken into account. Hoke et al. experimentally determined the convective heat transfer from a loop tubular geometry with wire fins [53], the typical ones of loop thermosyphons. Hence,

$$R^C_{conv} = \frac{1}{h_t \cdot A_t + \eta_w \cdot h_w \cdot A_w} \tag{33}$$

where h_t is the convective coefficient of the tubes, which is indeed derived from the wires' one according to Equation 34, A_t is the transmission area of the tubes, η_w is the fins efficiency (Equation 35), h_w is the convective coefficient of the wires derived from the Nusselt coefficient calculated with Equation 36 and A_w is the transmission area of the wires.

$$h_t = h_w \cdot \left(\frac{D_t}{D_w}\right)^{-0.5} \tag{34}$$

$$\eta_w = \frac{\tanh(m_w)}{m_w} \tag{35}$$

$$Nu = 0.027 \cdot Re^{0.819} \cdot [1 - 100 \cdot exp^{(-2.32 \cdot S_w/D_w)}] \tag{36}$$

3.4. Interconnection of Blocks

Next, it is necessary to consider different phenomena consequence of the interconnection between the different parts: thermal contacts and thermal bridge [54]. On the one hand, the former deals with the fact that when two surfaces are confronted, due to their roughness, the contact is not perfect, introducing air gaps that reduce heat transmission. Different materials such as thermal grease, graphite sheets, or even phase change materials are normally introduced in order to improve this contact. The value of the thermal resistance depends on the interface material and the pressure distribution, but it is estimated to be between 0.01 and 0.1 K/W per module [54, 55].

On the other hand, the latter can be defined as an area or component of an object which has higher thermal conductivity than the surrounding material, creating a path of least resistance for heat transfer [56]. In TEGs, the main sources for thermal bridges are the screws used to ensure a good contact and pressure distribution, and the direct heat transfer between the hot and cold heat exchanger, skipping the slim TEMs. Again, the value of this thermal resistance depends on the assembly, but as reference, it can be considered a value between 30 and 60 K/W [40].

3.5. Numerical Resolution

Once all the thermal resistances have been detailed, it is necessary to address the numerical resolution of the system, so that the temperature of each of the nodes can be obtained. As has been stated before, the thermal-electrical analogy is actually derived from the application of the implicit finite difference method to heat conduction equation. As a consequence, for each node i, considering a permanent regime, Equation 37 applies.

$$\sum_j \frac{T_j - T_i}{R_{ij}} + \dot{Q}_i = 0 \tag{37}$$

In this equation, i refers to the node under consideration, j to each adjacent node, T is their temperature, R_{ij} is the thermal resistance between nodes i and j, and $\dot{Q}_i$ is the heat flux generated or absorbed by node i. For an analogy with N nodes, a system of N equations with N unknowns is obtained.

In the present paper, the resolution of the former system of equations has been iterative. Thus, an initial temperature has been supposed for each node. Afterward, new temperatures have been calculated with Equation 37. The process has been iteratively repeated until the difference between the new and the last temperatures was lower than a tolerance. This tolerance has been defined to be 0.01.

4. Experimental Validation

In order to validate the computational model, the experiments performed by Catalan et al. have been used [20]. The present section first describes the prototype employed. Next, the results and analysis of the validation are presented.

4.1. Prototype description

Figure 3 depicts the GTEG with phase change heat exchangers developed and studied by Catalan et. al [20], based on which they concluded that this type of heat exchangers are the most suitable ones for GTEGs.

The hot side heat exchanger was a 1 m long stainless steel TPCT with a section of 60x60 mm^2 and a thickness of 5 mm. The used working fluid was water up to a height of 0.36 m. The squared section of this TPCT facilitated the installation of the TEMs. More specifically, two Marlow TG12-8-01L bismuth telluride modules were used [57].

Each TEM dissipated heat to an individual loop thermosyphon. In the considered experiments, two different geometries of loop thermosyphons were studied simultaneously, leading to a non-symmetrical generator. Hence, one of the TEMs dissipated heat to a loop thermosyphon with a condensation/convection area consisting of 8 levels of tubes, while the other one did it to a 6 levels loop thermosyphon. Otherwise, the thermosyphons were similar: the evaporator had an area of 50x50 mm^2, a width of 35 mm and a thickness of 2 mm; the internal working fluid was a mixture of water and ammonia; and the condensation/convection section was composed of two sets of 6 mm tubes with a length of 420 mm per level, with 1.5 mm wire fins separated 5 mm.

Figure 3: GTEG with phase change heat exchangers developed and studied by Catalan et. al [20].

4.2. Results and analysis

The experimental validation of the computational model has been performed on two steps. Firstly, only the cold side heat exchangers have been considered, measuring the capability of the model (blue block) to determine their thermal resistance for different heat fluxes. Secondly, the whole GTEG has been taken into consideration, leading to the validation of the whole computational model.

On the one hand, Figure 4 shows the results corresponding to the estimation of the thermal resistance of the cold side heat exchangers. The two different sizes of loop thermosyphons (8 and 6 levels) have been characterized for four heat fluxes. In the experiments, a heating plate was responsible for providing the desired heat flux $\dot{Q}$, and temperature at the base of the evaporator T_{ev} and in the climatic chamber T_{amb} were measured. Thus, thermal resistance was calculated as:

$$R = \frac{T_{ev} - T_{amb}}{\dot{Q}} = \frac{T_{ev} - T_{amb}}{V \cdot I} \tag{38}$$

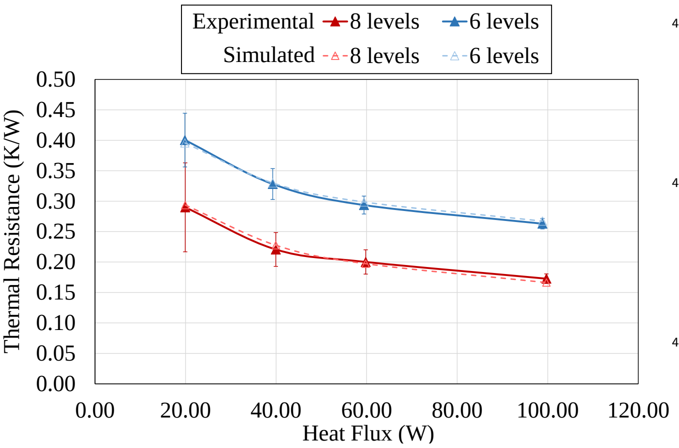

Figure 4: Experimental and simulated thermal resistance of the loop thermosyphons for different heat fluxes.

The experiments were repeated three times and the uncertainties calculated with [58], considering thermocouples with precision ±0.5 °C. The model is deterministic, so no variation of the results is expected. As it can be observed, as heat flux increases, the thermal resistance decreases. This is due to the fact that these heat exchangers are based on the phase change of an internal fluid, and the properties of this fluid improve with temperature. Besides, it can also be observed a lower thermal resistance with more number of levels. Since in loop thermosyphons all the convective area is effective for heat dissipation, heat flux is uniformly distributed among it, leading to lower thermal resistances with bigger convective areas. Due to this aspect, with this type of heat exchangers, it is possible to obtain low values of thermal resistance without the need for forced convection.

The discrepancy between the model and the experimental results has been estimated by means of the relative error (Equation 39).

$$Relative\ error = \frac{Value_{exp} - Value_{sim}}{Value_{exp}} \cdot 100 \qquad (39)$$

A statistical analysis of this relative error states that this sample can be described as a normal distribution with mean 0.26 and standard deviation 7.27. Therefore, the model predicts the thermal resistance of the loop thermosyphons with a relative error in the interval [−14.27 %; 14.81 %] in the 95 % of the cases. The wideness of this interval is mainly due to the big experimental uncertainties with low heat fluxes. If only the operating range between 40 and 100 W is considered, in which the GTEG will work, the relative error presents a normal distribution with mean −0.43 and standard deviation 4.32, leading to a relative error in the [−9.08 %; 8.21 %] interval in the 95 % of the cases.

On the other hand, once the cold side block had been validated, it was the turn of the whole GTEG. Since the prototype is non-symmetrical, being composed of two loop thermosyphons with different geometries, their thermal resistance is different, and so is the heat flux that goes through them. Therefore, it was necessary to adapt the developed computational model in order to correctly represent this behavior. Figure 5 depicts the thermal-electrical analogy, differentiating the two branches that represent each loop thermosyphon. The split point between them is located between the boiling and the condensation resistances of the hot side TPCT, which corresponds with the node at the internal saturation temperature T_{sat}. Due to the difficulties of simulating the real conditions of an HDR field at the laboratory, rope heaters directly in contact with the TPCT's evaporator were used as heat source. As a consequence, the model does not include the convective resistance R^{H}_{conv}.

The validation of the model has been performed by comparing two different parameters: power generation and temperature. Figure 6 shows the results corresponding to the estimation of power generation. More specifically, Figure 6(a) depicts the power generated by a TEM with a loop thermosyphon composed of 8 levels for heat dissipation, while Figure 6(b) does the same for a loop thermosyphon with 6 levels. In both cases, the values of power generation are shown for five different load resistances, and three temperatures of the heat source, maintaining the ambient temperature at 20 °C in all cases. As before, the experiments have been repeated three times and their uncertainties calculated, while the model is considered deterministic.

The maximum power generation is obtained with a load resistance of 3.2 Ω, whose value is similar to that of the internal electrical resistance of the TEM [57]. Moreover, this generation increases with higher heat source temperatures and lower thermal resistances of the cold side heat exchangers. Power generation depends on the temperature difference between the sides of the TEMs, and in order to increase this temperature difference, high temperature heat sources and heat exchangers with low thermal resistances are needed. Since the 8 levels loop thermosyphon had a lower thermal resistance in comparison with the 6 levels one, the generation obtained in the left graph is higher than in the right one.

The comparison between the experimental results and the model predictions reveals a good concordance except for the values for 1.43 Ω, for which the model estimates a generation higher than in reality, but still encompassed in the uncertainty ranges. Figure 7(a) graphs the power estimated by the model versus the experimentally measured one. All the values are encompassed in a ±6 % range, except those for 1.43 Ω that enlarge the positive range to +25 %. The problem with relative deviations is that they soar for small values. The maximum absolute error is actually 0.34. If, as before, the discrepancy between the model and the experimental results is estimated by means of the relative error (Equation 39) and a statistical analysis is made, the total mean error is −3.4 considering all values. When neglecting those corresponding to 1.43 Ω, the errors follow a normal distribution with mean −0.28

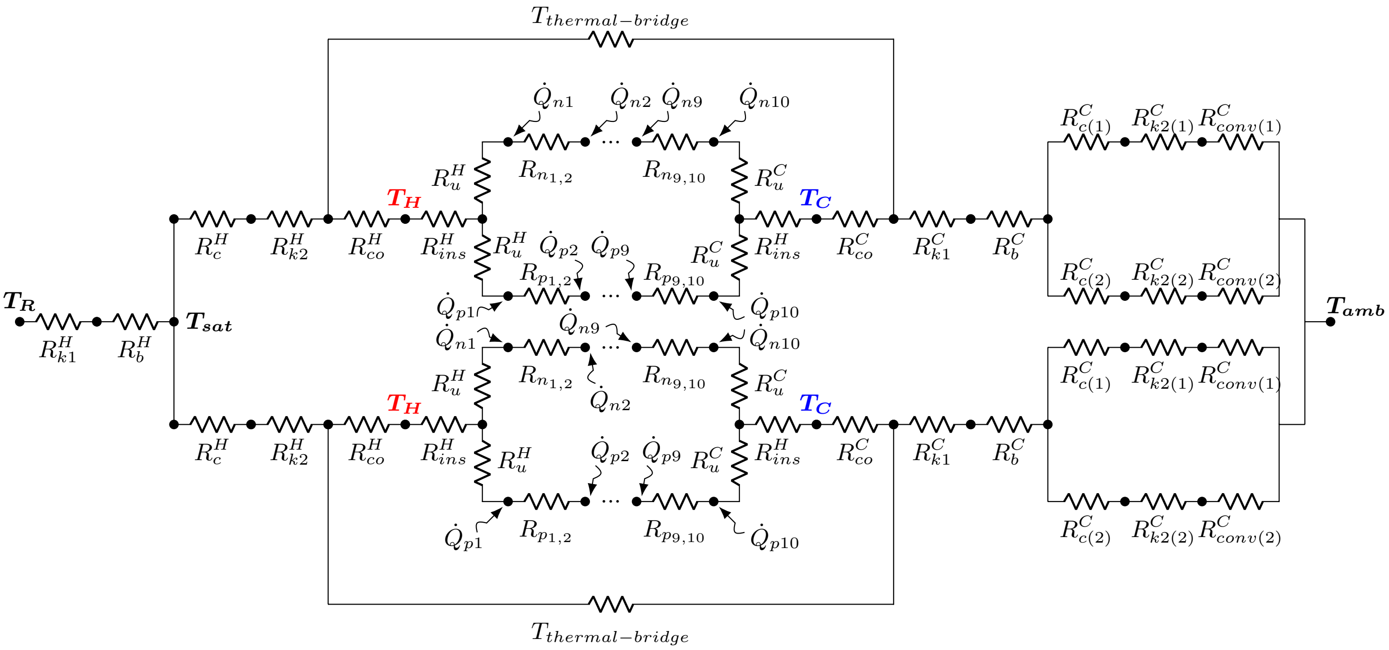

Figure 5: Thermal-electrical analogy used in the experimental validation.

and standard deviation 1.42. In the study of the next section, which serves to achieve the objective of this paper, generation will be always calculated with the load resistance that maximizes generation, for which the model is considered accurate enough.

A similar study has been performed for the temperature distribution. Hence, since the comparison of temperatures cannot be done in absolute values, the temperature difference of the hot and the cold side heat exchanger has been compared (HHE and CHE respectively). Figure 7(b) graphs the estimated temperature differences versus the experimental ones. As it can be observed, there is a good concordance in the data, which is encompassed, in all cases, in the $\pm 8\,\%$ range. A statistical analysis of the relative errors (Equation 39) reveals that they follow a normal distribution with a mean of 0.18 and a standard deviation of 3.06. Thus, it is demonstrated that the model has been validated both for optimal generation and temperature distribution, leading to a competent tool for the analysis of the operation of GTEGs, as it is developed in the next section.

5. Computational study of a GTEG at Timanfaya National Park

Based on the developed and validated model, the present section focuses on the analysis of the influence of different parameters on a GTEG considering a real location: Timanfaya National Park (Canary Islands, Spain), whose potential will also be estimated. Taking into account that it is a nature reserve, it will be important to maximize the power produced per thermoelectric generator, minimizing the number of boreholes required, as well as using water as the internal working fluid, so that the environmental impact is minimal.

Timanfaya National Park hosts one of the world's greatest shallow HDR field, both in intensity and extension. There are 11 700 m^2 of geothermal anomalies presenting temperatures of more than 200 °C at ground level and 615 °C at a depth of 5-15 m [32, 59, 60]. The origin of these anomalies is believed to be a body of lava from the last eruptions in 1730-36 and 1824, which has not reached the surface and is slowly cooling down.

Due to the low thermal diffusivity of the superficial hot rocks ($8 \cdot 10^{-4} \text{cm}^2/\text{s}$), which complicates the heat transfer by conduction and causes a slow recovery of the system, heat extraction mechanism needs to be convection [32]. Based on this statement, different experiments intended to evaluate the gas fluxes that ascend from the geothermal anomalies were performed, for which eight 60 m long boreholes were drilled in 1991 and 1992 [59]. Within the park, two different areas were studied: *Islote Hilario*, with 3000 m^2, is the area with the highest temperatures and air velocities, while *Casa de los Camelleros*, with 2000 m^2, although presents lower temperatures, it is still considered a high temperature geothermal field. Table 1 details the air velocity and ground temperatures at different depths characteristics of each site. These values were measured again in January 2019, so that it was verified that the system had not cooled down since the last measurements in the 1990s.

For each of the considered locations, the computational model depicted in Figure 2 has been used to perform the computational study. The geometries taken as reference derive from constructional aspects. Hence, for *Islote Hilario*, due to its high temperatures and due to the limita-

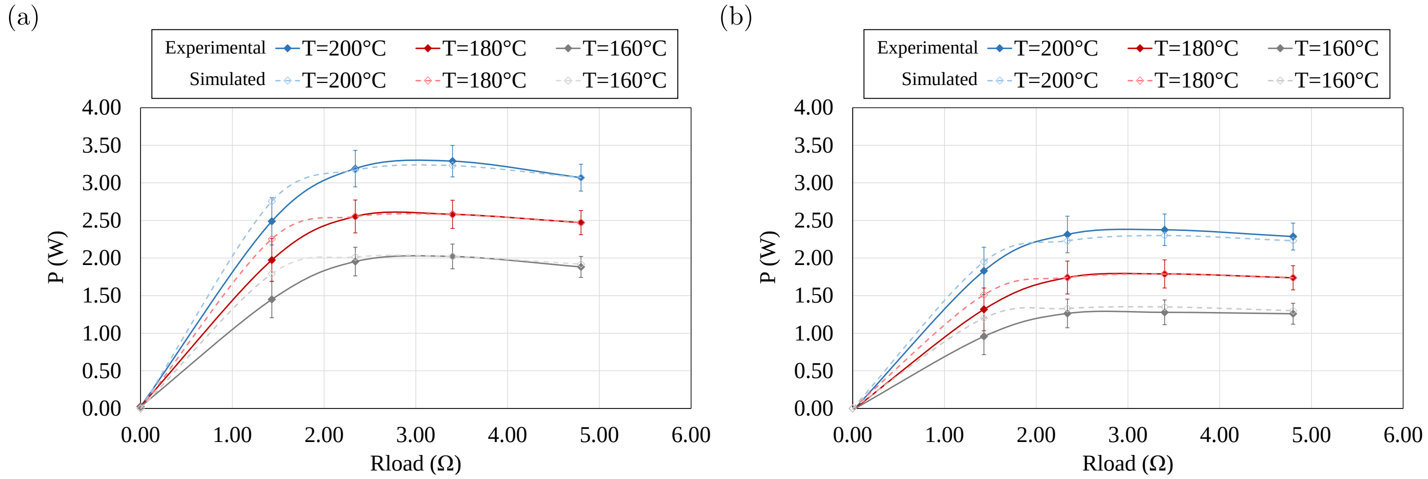

Figure 6: Experimental and simulated power generated per module for different load resistances and heat source temperatures (a) considering an 8 levels loop thermosyphon as cold side heat exchanger and (b) considering a 6 levels one.

Table 1: Air velocity and ground temperatures at different depths characteristics of the two areas of study within Timanfaya National Park.

	Casa de los Camelleros	Islote Hilario
v_{air} (m/s)	6.03	11.15
T at surface (°C)	200	480
T at 0.75 m (°C)	205	490
T at 1.125 m (°C)	207	495
T at 2.25 m (°C)	210	510

tions of both the critical temperature of water, the used working fluid, and the maximum temperature supported by Bi-Te TEMs (250 °C), the hot side TPCT is a stainless steel finless tube with a diameter of 48 mm and a thickness of 5 mm. In the case of *Casa de los Camelleros*, the TPCT is a 46 mm aluminum tube, 3.25 mm thick, with 31 vertical fins with a length of 17 mm and a thickness of 2 mm. In both cases, it is considered that water fills half of the inserted length of the TPCT. The variables of study, apart from the location, are: the inserted length of the TPCT (that determines the input temperature of the gases T_G), the size of the cold side thermosyphon (considering the two studied geometries of 8 and 6 levels loop thermosyphons), and the number of thermoelectric modules (TEMs). As before, each TEM incorporates an individual cold side loop thermosyphon.

The temperature of the gases T_G, which is one of the inputs of the model, is considered constant and with a value equal to the average temperature of the evaporator. Thus, for a TPCT inserted 3 m, whose evaporator measures 1.5 m, the input temperature is the value at a depth of 2.25 m. On the ambient side, the average temperature and wind velocity of the park, 20.8 °C and 5.43 m/s, have been taken as reference [62]. Regarding the contact between the different parts, per each module, a thermal contact resistance of 0.05 K/W and a thermal bridge resistance of 41.6 K/W have been considered [54, 55].

Figure 8 depicts the power generated (left axis) and the efficiency (right axis) of GTEGs working with the optimal load resistance in *Islote Hilario*, considering a different number of TEMs, three inserted lengths of the hot side TPCT, and two sizes of cold side loop thermosyphons, with an 8 levels loop thermosyphon in Figure 8(a) and a 6 levels one in Figure 8(b). As can be observed, in all cases the efficiency of the generator decreases as the number of modules increases. This efficiency is higher with longer TPCTs, since the evaporator is larger and therefore convective R^H_{conv}, conductive R^H_{k1} and boiling R^H_b thermal resistances decrease (Equation 1,4,5,6) increasing the heat flux, as well as because of slightly higher air temperatures deeper in the boreholes. Thus, the temperature between the sides of the TEMs is higher, and so is their efficiency. This also occurs with lower thermal resistances of the cold side heat exchanger, leading to higher efficiencies in the case of the 8 levels loop thermosyphon.

Regarding total power generation, similarly to efficiency, with longer TPCTs and bigger loop thermosyphons, i.e. lower thermal resistances, more power is generated. Nonetheless, in this case, the variation with respect to the number of TEMs is different. Despite the continuous reduction of efficiency, in the beginning, when more TEMs are added, total generation of the GTEGs increases until an optimum point is reached, from which generation starts to decrease. This is due to the fact that the TEMs share a unique TPCT. Hence, the thermal resistances of convection with the hot geothermal gases, conduction in the evaporator, and boiling remain constant regardless of the number of TEMs. The rest of the thermal resistances of the thermal-electrical analogy of Figure 2 decrease with more TEMs. Since each added TEM has its own cold side heat exchanger, the value of these resistances divides

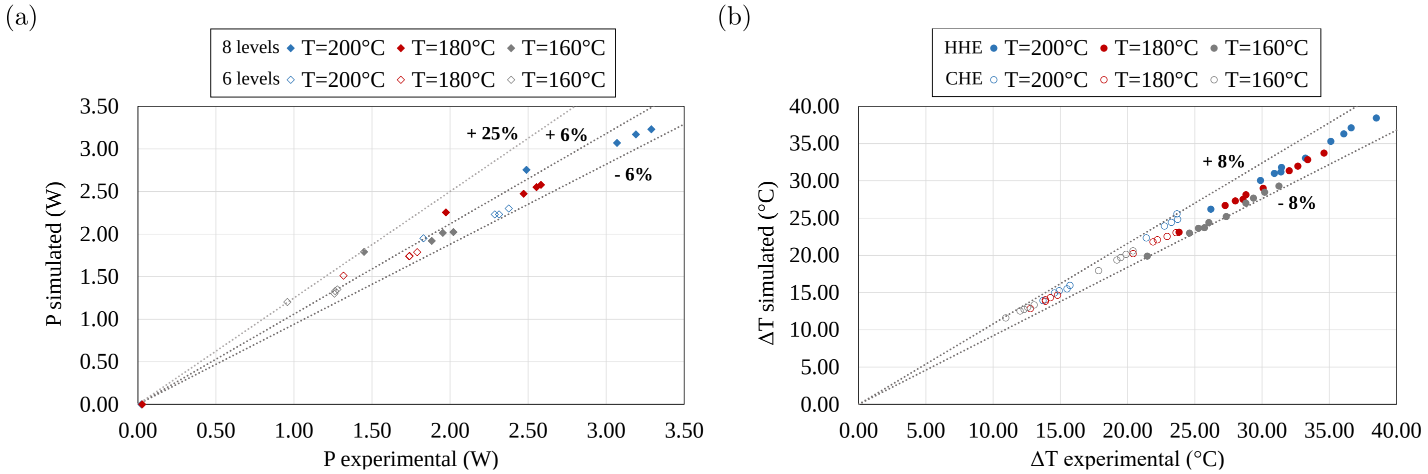

Figure 7: (a) Simulated power generation versus real one, for different temperatures of the heat source and the two different geometries of loop thermosyphons studied, and (b) Simulated versus real temperature difference of the hot and cold side heat exchangers (HHE and CHE respectively) for different temperatures of the heat source.

by the number of TEMs due to their parallel connection, leading to a lower global thermal resistance. As a consequence, more heat flux is absorbed by the GTEG and the temperature of the hot side of the TEMs decreases.

This reduction can be observed in Figure 9(a), which shows the temperatures of the gases T_G, the saturation of the internal working fluid T_{sat} (which never exceeds the critical value for water), the hot and the cold side of the modules T_H and T_C, and the ambient temperature T_{amb} for the case of a TPCT inserted 3 m in the ground and with 8 levels loop thermosyphons as cold side heat exchangers. As the number of TEMs increases, the temperature difference between the sides of the TEMs decreases, mainly due to the reduction of the hot side temperature. As a consequence, the efficiency decreases. Nonetheless, there is an optimum point where there exists an equilibrium between the number of TEMs and the decreased efficiency. Given a fixed size of the cold side loop thermosyphon, this optimum point occurs with more TEMs as the thermal resistances R^H_{conv}, R^H_{k1} and R^H_b decrease with longer inserted lengths of the TPCT. This is due to the fact that the power generated per module decreases at a slower rate with the addition of TEMs for lower resistances, as can be observed in the decrease of efficiency, moving the optimum point from 6 TEMs in the case of 1 m inserted, to 8 TEM for 1.5 m and to 16 TEMs for 3 m. The same optimum points are obtained for GTEGs with 6 levels loop thermosyphons. Considering all the studied cases, the optimal GTEG for *Islote Hilario* generates 68.07 W with 16 TEMs, when the inserted length of the hot side TPCT is 3 m and 8 levels loop thermosyphons are used as cold side heat exchangers.

In *Casa de los Camelleros* (from now on, Camelleros), due to the lower temperature of the gases, which made it impossible to exceed neither the critical point of water nor the maximum temperature stood by the modules, vertical fins were added in the external part of the evaporator. As it can be seen in Figure 9(b), the addition of fins considerably improves the heat transfer between the gases and the TPCT, reducing its thermal resistance and leading to a smaller temperature difference between the gases and the hot side of the modules, a difference which also increases with more TEMs.

Figure 10 depicts the power (with an optimal load resistance) and the efficiency with respect to the number of TEMs for all the studied geometries, which follow a similar trend that in *Islote Hilario*. The main difference between the two locations is that, for each geometry, the optimal generator of *Camelleros* is composed of a higher number of TEMs than in *Islote Hilario*. Due to the addition of fins, the thermal resistance of the hot side has diminished, causing a slower decreasing rate in the power generated per module with the addition of TEMs and shifting the optimum point to the right of the graph. Hence, for the case of having 8 levels loop thermosyphons in the cold side, the optimal GTEG is composed of 10 TEMs for 1 m inserted, 14 TEMs for 1.5 m and 28 for 3 m. Furthermore, in contrast to *Islote Hilario*, in this case there does exist a difference with the size of the cold side heat exchanger, since the thermal resistance of the hot side has less weight in the global thermal resistance. Thus, when having 6 levels loop thermosyphons at the cold side, the optimal GTEG is achieved with 30 TEMs for 3 m. The higher thermal resistance of the 6 levels loop thermosyphons causes a more noticeable decrease of the global cold side thermal resistance with the increase of TEMs, leading to a slower decrease of efficiency that, due to a smaller decrease in the power generated per TEM, provokes that the optimum point is achieved with more TEMs. Among all the studied cases, in *Camelleros* the optimal GTEG is again inserted 3 m in the ground and incorporates 8 levels loop thermosyphons as cold side heat exchangers. The maximum generation of

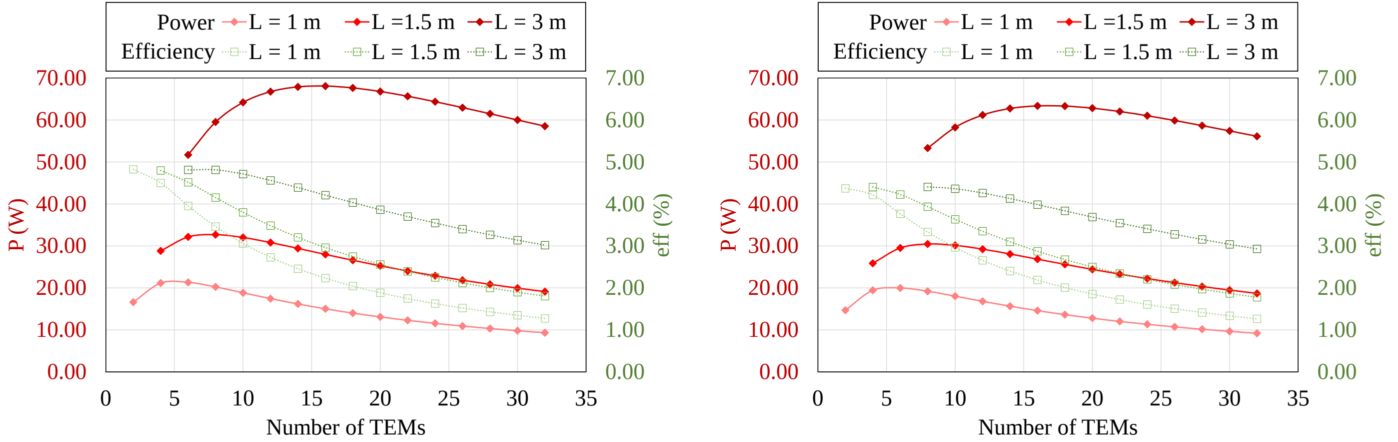
(a) Islote Hilario. 8 levels loop thermosyphon.

(b) Islote Hilario. 6 levels loop thermosyphon.

Figure 8: Power generated (left axis) and efficiency (right axis) of GTEGs in *Islote Hilario*, considering a different number of TEMs, three inserted lengths of the hot side TPCT, and two sizes of loop thermosyphons: (a) with 8 levels and (b) with 6 levels.

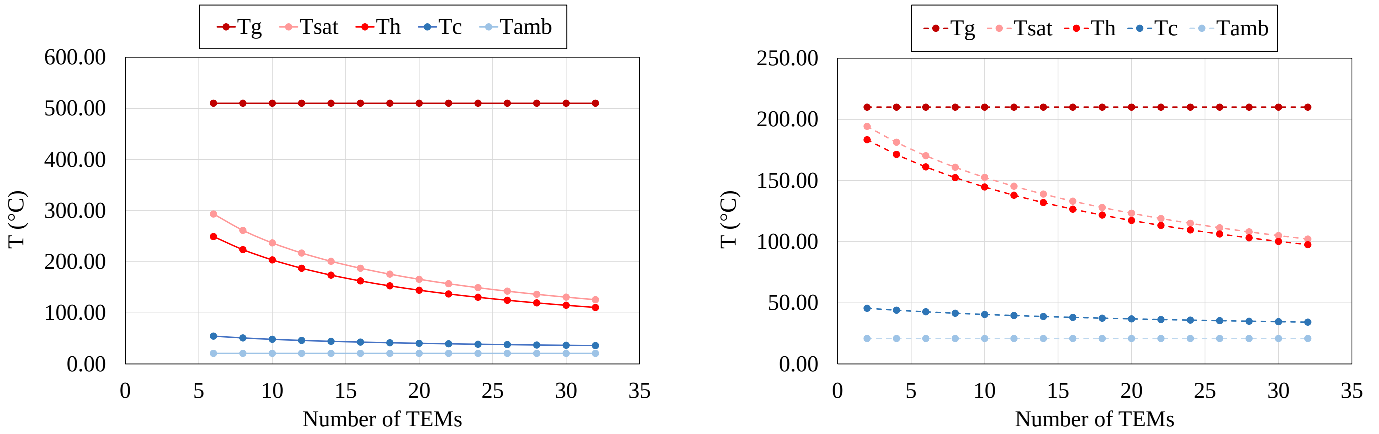
(a) Islote Hilario. 8 levels LT. TPCT inserted 3 m.

(b) Camelleros. 8 levels LT. TPCT inserted 3 m.

Figure 9: Temperature distribution of the gases T_G, saturation of the internal working fluid T_{sat}, the hot and cold side of the modules T_H and T_C, and the ambient T_{amb} for a GTEG composed of a TPCT inserted 3 m and an 8 levels loop thermosyphons, located at (a) *Islote Hilario* or (b) *Casa de los Camelleros*.

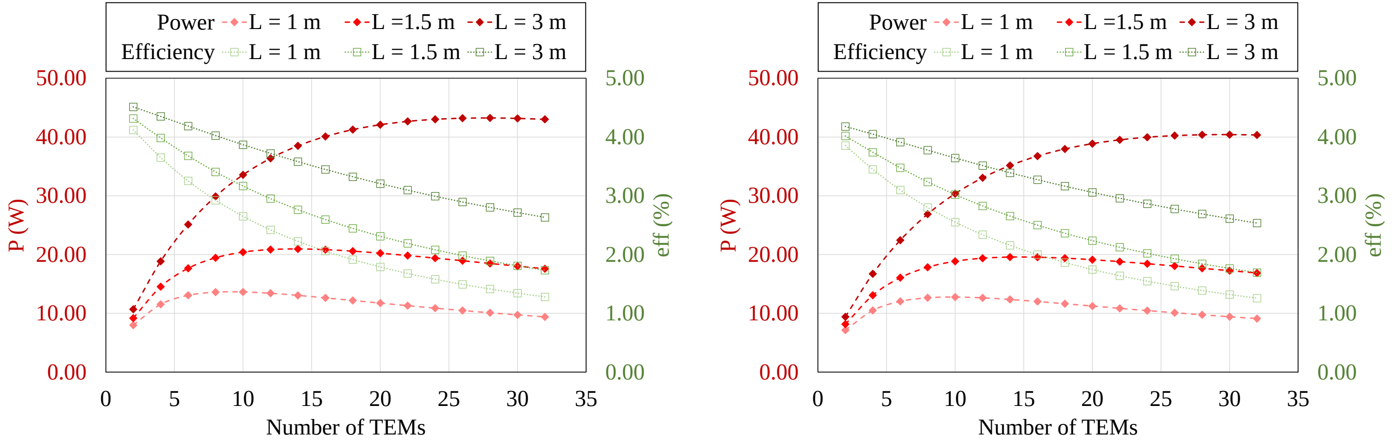
(a) Camelleros. 8 levels loop thermosyphon.

(b) Camelleros. 6 levels loop thermosyphon.

Figure 10: Power generated (left axis) and efficiency (right axis) of GTEGs in *Casa de los Camelleros*, considering a different number of TEMs, three inserted lengths of the hot side TPCT, and two sizes of loop thermosyphons: (a) with 8 levels and (b) with 6 levels.

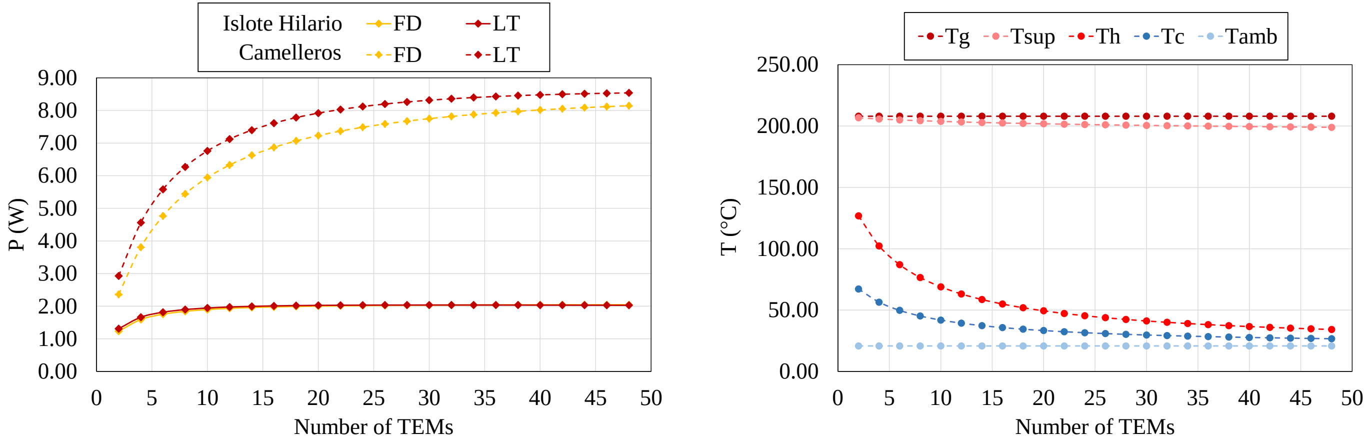
(a) Solid bar inserted 3 m.

(b) Camelleros. Solid bar inserted 3 m. FD.

Figure 11: (a) Power generated by GTEGs composed of a solid bar inserted 3 m in the ground as hot side heat exchanger, and fin dissipators (FD) or 8 levels loop thermosyphons (LT) as cold side ones. (b) Temperature distribution of the gases T_G, superficial temperature T_{sup}, the hot and cold side of the modules T_H and T_C, and the ambient T_{amb} for a GTEG composed of a solid bar inserted 3 m and fin dissipators, located at *Casa de los Camelleros.*

this device is 43.23 W, achieved with 28 TEMs.

Instead of using phase change heat exchangers, an alternative configuration that also fulfills the requirements of robustness and absence of both moving parts and auxiliary consumption, but it is simpler, would have been solid heat exchangers. Hence, for the hot side heat exchanger the easiest option would consist of a solid bar of a metallic material, with suitable conductive properties; and for the cold side ones, fin dissipators (FD). Figure 11(a) shows, in yellow, the generation obtained with a thermoelectric generator with the former configuration for the two considered locations: *Islote Hilario* with filled lines, and *Camelleros* with dashed ones. More specifically, the hot side heat exchangers present the same geometry and material than their equivalent TPCT, considering an inserted length of 3 m since it led to the best results. Each cold side heat exchanger is the fin dissipator characterized by Catalan et al., which presents a thermal resistance of 0.745 K/W under breeze conditions [20]. In order to simulate these results with the computational model, at the hot side heat exchanger only convective and conductive resistances have been taken into account, and in the cold side two fin dissipators per level with a separation of 25 cm between levels have been considered.

As it can be observed, as more TEMs are added, generation continuously increases. In this case, generation per level is practically constant, with a value that is higher for lower levels since its conductive thermal resistance is smaller. Hence, when more levels are added, more generation is obtained, although the increase in the total power generated gradually slows down with the addition of TEMs, stabilizing at a certain value when adding more TEMs barely increases generation. Nevertheless, in comparison with GTEGs with only phase change heat exchangers, there exists a huge detriment in the generation. In *Islote Hilario*, generation stabilizes at around 2 W, while in *Camelleros* at 8.2 W, 97% and 81% lower than the maximum values obtained previously. This reduction is caused by the enormous thermal resistance of the solid hot side heat exchanger. In Figure 11(a) the generation obtained with 8 levels loop thermosyphons (LT) has also been depicted in addition to the values with fin dissipators (FD). Thus, although there exists a slight increase, the generation still shows a considerable reduction: 2 and 8.5 W respectively, confirming that the hot side heat exchanger is responsible for the detriment. The greater reduction in *Islote Hilario* is due to the low thermal conductivity of stainless steel, which is used because of the really high temperatures that exist in this location, and that other more conductor metals such as aluminum or copper would not resist.

The main component of the thermal resistance of the solid hot side heat exchanger is due to the conductive part. Figure 11(b) depicts, for *Camelleros*, the temperatures of the geothermal gases T_G, the superficial temperature of the hot side heat exchanger T_{sup}, the hot and cold sides of the thermoelectric modules T_h and T_c, and the ambient temperature T_{amb}. Hence, while the superficial temperature is very close to the gases' one, it can be seen that the principal temperature drop occurs in the conductive part. This drop increases with a higher number of TEMs, since apart from the effect of adding more modules to a unique hot side heat exchanger, the length of the bar outside the ground increases maintaining the same area and thermal conductivity. Hence, the decrease in the temperatures with the number of TEMs is more drastic than when having a TPCT. In *Islote Hilario*, although not represented, due to the lower thermal conductivity of stainless steel, the temperature difference is even higher and the reduction with the addition of TEMs is more severe.

Table 2: Monthly analysis of the energy generated by the optimized GTEGs in each of the studied locations, showing also relevant operating information.

Location	Month	T_{amb} (°C)	v_{air} (m/s)	T_G (°C)	T_H (°C)	T_C (°C)	R_{HHE} (K/W)	R_{CHE} (K/W)	P (W)	η (%)	Energy (kWh)	Energy (kWh/year)
ISLOTE HILARIO	January	17.3	5.4	510.00	159.75	38.77	3.29	0.17	70.35	4.32	52.34	601.36
	February	17.7	5.5	510.00	159.94	39.05	3.29	0.16	70.20	4.31	47.17	
	March	18.8	5.4	510.00	160.60	40.03	3.29	0.16	69.64	4.28	51.81	
	April	19.2	5.7	510.00	160.77	40.28	3.29	0.16	69.50	4.28	50.04	
	May	20.4	5.4	510.00	161.55	41.44	3.29	0.16	68.85	4.25	51.22	
	June	22.1	5.5	510.00	162.50	42.85	3.29	0.16	68.05	4.21	49.00	
	July	23.4	6.4	510.00	163.08	43.71	3.29	0.16	67.57	4.19	50.27	
	August	24.6	6.1	510.00	163.83	44.83	3.29	0.15	66.94	4.16	49.81	
	September	24.3	4.9	510.00	163.95	45.00	3.29	0.16	66.85	4.15	48.13	
	October	22.9	4.6	510.00	163.23	43.94	3.29	0.16	67.45	4.18	50.18	
	November	20.6	5.1	510.00	161.73	41.71	3.29	0.16	68.69	4.24	49.46	
	December	18.4	5.2	510.00	160.43	39.78	3.29	0.16	69.78	4.29	51.92	
CAMELLEROS	January	17.3	5.4	210.00	104.21	31.87	1.70	0.20	45.27	2.98	33.68	380.95
	February	17.7	5.5	210.00	104.39	32.18	1.70	0.20	45.09	2.97	30.30	
	March	18.8	5.4	210.00	104.95	33.14	1.70	0.20	44.52	2.95	33.12	
	April	19.2	5.7	210.00	105.12	33.43	1.70	0.20	44.35	2.94	31.93	
	May	20.4	5.4	210.00	105.75	34.54	1.70	0.20	43.69	2.91	32.51	
	June	22.1	5.5	210.00	106.58	35.97	1.70	0.19	42.85	2.88	30.85	
	July	23.4	6.4	210.00	107.15	36.94	1.70	0.19	42.29	2.86	31.46	
	August	24.6	6.1	210.00	107.78	38.03	1.70	0.19	41.66	2.83	30.99	
	September	24.3	4.9	210.00	107.77	38.01	1.70	0.19	41.67	2.83	30.00	
	October	22.9	4.6	210.00	107.12	36.89	1.70	0.20	42.32	2.86	31.48	
	November	20.6	5.1	210.00	105.89	34.77	1.70	0.20	43.56	2.91	31.36	
	December	18.4	5.2	210.00	104.78	32.85	1.70	0.20	44.69	2.95	33.25	

Consequently, it becomes patent that in order to have a robust GTEG without moving parts nor auxiliary consumption, the best configuration is composed of phase change heat exchangers, reaffirming the novelty proposed in the present paper.

Considering the optimal GTEG with phase change heat exchangers of each location and taking into account the monthly average temperature and wind velocity of Timanfaya National Park [62, 63], Table 2 analyses the energy that can be produced per year with each GTEG. For more information, the most significant temperatures, the thermal resistances of the hot and cold side heat exchangers (R_{HHE} and R_{CHE}), the power generated and its efficiency are also depicted. As it can be observed, the weather at Timanfaya National Park is quite stable all year long, with average temperatures between 17.3 and 24.6 °C and wind velocities in the range from 4.6 to 6.4 m/s. As a consequence, the operation parameters of the GTEG remain practically constant during all months, and there is only 3.5 W of difference between the month with the highest generation (January) and the one with the lowest (September in *Islote Hilario* and August in *Camelleros*).

The GTEG of *Islote Hilario* operates with an average temperature difference in the TEMs of 120 °C, with approximately 162 °C in the hot side and 42 °C in the cold one, leading to an average power of 68.66 W. Given that the temperature of the geothermal gases is 510 °C, it is remarkable to note the big temperature loss that occurs in the hot side heat exchanger, which presents a value of 3.29 K/W per module, much higher than the cold side one of 0.16 K/W. In the case of *Camelleros*, the hot side heat exchanger has a considerably lower thermal resistance due to the addition of fins. As a consequence, the temperature difference in this heat exchanger is of just 101 °C approximately. In this case, the TEMs operate with an average temperature difference of 71 °C, leading to an average generated power of 43.5 W. Since geothermal energy is always available, GTEGs can generate energy permanently, during the 8760 hours of a year. Hence, in *Islote Hilario* each GTEG annually generates 601.36 kWh and in *Camelleros*, 380.95 kWh are generated per device.

Finally, taking into account the extension of each area (3000 m^2 in *Islote Hilario* and 2000 m^2 in *Camelleros*), an extrapolation of total energy generation can be performed. It was estimated that 438.51 and 427.55 W/m^2 can be respectively extracted in these areas without affecting the geothermal field [59]. Therefore, up to 470.87 MWh can be generated in *Islote Hilario*, and 210.66 MWh in *Casa de los Camelleros*, leading to a total annual electricity generation of 681.53 MWh.

6. Conclusions

In conclusion, the present paper has delved into the study of geothermal thermoelectric generators (GTEGs) with phase change heat exchangers, demonstrating the potential of the solution for hot dry rock (HDR) fields with a minimal environmental impact. For this purpose, a computational model based on the thermal-electrical analogy has been developed and validated thanks to an experimental prototype, leading to an error estimating the generation in the maximum point of less than 6 %, and of 8 % in case of the prediction of the temperature differences in the heat exchangers.

Based on the model, a computational study of GTEGs has been performed for two areas within Timanfaya National Park (Canary Islands, Spain): *Islote Hilario*, where gases emerge at around 500 °C and more than 11 m/s; and *Casa de los Camelleros*, with 200 °C and 6 m/s respectively. The designed GTEGs are composed of a two phase closed thermosyphon (TPCT) with water as working fluid as hot side heat exchanger, and loop thermosyphons (one per thermoelectric module) as cold side ones. This configuration leads to a device without moving parts nor auxiliary consumption, resulting in a robust generator that maximizes net generation. In the study, the size of the heat exchangers, the number of thermoelectric modules (TEMs), and the addition or not of fins have been considered.

As a result, it has arisen the importance of using heat exchangers with low thermal resistance in order to maximize power generation. The lower the thermal resistance of the heat exchangers, the higher the generation. Nonetheless, since all the TEMs share a common TPCT, there exists an optimum in the generation. In the case of *Islote Hilario*, the optimized GTEG generates 68.07 W with 16 TEMs, while in *Casa de los Camelleros*, the optimum number of TEMs is 28, which leads to a generation of 43.23 W. If a solid bar had been used as hot side heat exchanger and fin dissipators as cold side ones, generation will respectively be 97% and 81% lower, thus reaffirming that passive heat exchangers based on phase change are the most adequate ones for GTEGs. Thanks to these GTEGs and their scalability, it would be possible to generate 681.53 MWh of electricity in one year.

Acknowledgments

We would like to acknowledge the support of the Spanish State Research Agency and FEDER–UE under the grant RTC-2017-6628-3; as well as the FPU Program of the Spanish Ministry of Science, Innovation, and Universities (FPU16/05203).

References

[1] W. Zuo, Q. Li, Z. He, Y. Li, Numerical investigations on thermal performance enhancement of hydrogen-fueled micro planar combustors with injectors for micro-thermophotovoltaic applications, Energy 194 (2020) 116904. doi:10.1016/j.energy.2020.116904.

[2] Q. Li, W. Zuo, Y. Zhang, J. Li, Z. He, Effects of rectangular rib on exergy efficiency of a hydrogen-fueled micro combustor, International Journal of Hydrogen Energy 45 (16) (2020) 10155–10163. doi:10.1016/j.ijhydene.2020.01.221.

[3] W. Zuo, J. Li, Y. Zhang, Q. Li, S. Jia, Z. He, Multi-factor impact mechanism on combustion efficiency of a hydrogen-fueled micro-cylindrical combustor, International Journal of Hydrogen Energy 45 (3) (2020) 2319–2330. doi:10.1016/j.ijhydene.2019.11.012.

[4] REN21. Renewables Now, Why is renewable energy important? URL https://www.ren21.net/why-is-renewable-energy-important/

[5] REN21, Renewables 2019 Global Status Report, Tech. rep., Paris (2019).

[6] K. Li, H. Bian, C. Liu, D. Zhang, Y. Yang, Comparison of geothermal with solar and wind power generation systems, Renewable and Sustainable Energy Reviews 42 (2015) 1464–1474. doi:10.1016/j.rser.2014.10.049.

[7] D. Astrain, J. G. Vián, A. Martínez, A. Rodríguez, Study of the influence of heat exchangers' thermal resistances on a thermoelectric generation system, Energy 35 (2) (2010) 602–610. doi:10.1016/j.energy.2009.10.031.

[8] A. Elghool, F. Basrawi, T. K. Ibrahim, K. Habib, H. Ibrahim, D. M. N. D. Idris, A review on heat sink for thermo-electric power generation: Classifications and parameters affecting performance, Energy Conversion and Management 134 (2017) 260–277. doi:10.1016/j.enconman.2016.12.046.

[9] K. Wang, J. Liu, X. Wu, Downhole geothermal power generation in oil and gas wells, Geothermics 76 (October) (2018) 141–148. doi:10.1016/j.geothermics.2018.07.005.

[10] K. Wang, X. Wu, Downhole thermoelectric generation in unconventional horizontal wells, Fuel 254 (March) (2019) 115530. doi:10.1016/j.fuel.2019.05.113.

[11] C. Suter, Z. R. Jovanovic, A. Steinfeld, A 1kWe thermoelectric stack for geothermal power generation - Modeling and geometrical optimization, Applied Energy 99 (2012) 379–385. doi:10.1016/j.apenergy.2012.05.033.

[12] C. Suter, Z. Jovanovic, A. Steinfeld, A 1 kWel thermoelectric stack for geothermal power generation-Modeling and geometrical optimization, AIP Conference Proceedings 1449 (2012) 540–543. doi:10.1063/1.4731613.

[13] C. Liu, P. Chen, K. Li, A 1 KW Thermoelectric Generator for Low-temperature Geothermal Resources, in: Thirty-Ninth Workshop on Geothermal Reservoir Engineering, no. 2001, 2014, pp. 1–12.

[14] C. Liu, P. Chen, K. Li, Geothermal Power Generation Using Thermoelectric Effect, GRC Transactions 37 (2013).

[15] C. Liu, P. Chen, K. Li, A 500 W low-temperature thermoelectric generator: Design and experimental study, International Journal of Hydrogen Energy 39 (28) (2014) 15497–15505. doi:10.1016/j.ijhydene.2014.07.163.

[16] X. Niu, J. Yu, S. Wang, Experimental study on low-temperature waste heat thermoelectric generator, Journal of Power Sources 188 (2) (2009) 621–626. doi:10.1016/j.jpowsour.2008.12.067.

[17] R. Ahiska, H. Mamur, Design and implementation of a new portable thermoelectric generator for low geothermal temperatures, IET Renewable Power Generation 7 (6) (2013) 700–706. doi:10.1049/iet-rpg.2012.0320.

[18] R. Ahiska, H. Mamur, Development and application of a new power analysis system for testing of geothermal thermoelectric generators, International Journal of Green Energy 13 (7) (2016) 672–681. doi:10.1080/15435075.2015.1017102.

[19] A. Banerjee, T. Chakraborty, V. Matsagar, Evaluation of possibilities in geothermal energy extraction from oceanic crust using offshore wind turbine monopiles, Renewable and Sustainable Energy Reviews 92 (May) (2018) 685–700. doi:10.1016/j.rser.2018.04.114.

[20] L. Catalan, P. Aranguren, M. Araiz, G. Perez, D. Astrain, New opportunities for electricity generation in shallow hot dry rock fields: A study of thermoelectric generators with different heat exchangers, Energy Conversion and Management 200 (2019) 112061. doi:10.1016/j.enconman.2019.112061.

[21] D. Brown, The Enormous Potential for Hot Dry Rock Geothermal Energy, in: Mining the Earth's Heat: Hot Dry Rock Geothermal Energy, Springer-Verlag, Berlin Heidelberg, 2012, Ch. 2. arXiv:1107.2286, doi:10.1007/978-3-.

[22] M. F. Remeli, L. Tan, A. Date, B. Singh, A. Akbarzadeh, Simultaneous power generation and heat recovery using a heat pipe assisted thermoelectric generator system, Energy Conversion and Management 91 (2015) 110–119. doi:10.1016/j.enconman.

2014.12.001.

[23] P. Aranguren, D. Astrain, A. Rodriguez, A. Martinez, Net thermoelectric power generation improvement through heat transfer optimization, Applied Thermal Engineering 120 (2017) 496–505. doi:10.1016/j.applthermaleng.2017.04.022.

[24] F. Brito, L. Goncalves, J. Martins, N. Antunes, D. Sousa, Thermoelectric exhaust heat recovery with heat pipe-based thermal control, Journal of Electronic Materials (2015).

[25] N. Pacheco, F. P. Brito, R. Vieira, J. Martins, H. Barbosa, L. M. Goncalves, Compact automotive thermoelectric generator with embedded heat pipes for thermal control, Energy 197 (2020) 117154. doi:10.1016/j.energy.2020.117154.

[26] B. Orr, A. Akbarzadeh, M. Mochizuki, R. Singh, A review of car waste heat recovery systems utilising thermoelectric generators and heat pipes, Applied Thermal Engineering 101 (2016) 490–495. doi:10.1016/j.applthermaleng.2015.10.081.

[27] A. Date, A. Date, C. Dixon, A. Akbarzadeh, Theoretical and experimental study on heat pipe cooled thermoelectric generators with water heating using concentrated solar thermal energy, Solar Energy 105 (2014) 656–668. doi:10.1016/j.solener.2014.04.016.

[28] Y. Huang, W. Li, D. Xu, Y. Wu, Spatiotemporal rule of heat transfer on a soil/finned tube interface, Sensors (Switzerland) 19 (5) (2019). doi:10.3390/s19051159.

[29] Y. Huang, D. Xu, J. Kan, W. Li, Study on field experiments of forest soil thermoelectric power generation devices, PLoS ONE 14 (8) (2019) 1–13. doi:10.1371/journal.pone.0221019.

[30] R. Dell, R. Unnthorsson, C. Wei, G. Sidebotham, M. Jonsson, W. Foley, E. Ginzburg, S. Paul, S. Kim, A. Morris, Thermoelectric-based power generator for powering microcontroller based security camera, in: ASME International Mechanical Engineering Congress and Exposition, 2012, pp. 635–642.

[31] R. Dell, C. S. Wei, M. T. Petralia, G. Gislason, R. Unnthorsson, Thermoelectric Powered Security Systems in Iceland Using a Geothermal Steam Pipe as a Heat Source, Proceedings 2 (8) (2018) 440. doi:10.3390/ICEM18-05309.
URL http://www.mdpi.com/2504-3900/2/8/440

[32] J. Diez-Gil, V. Araña, R. Ortiz, J. Yuguero, Stationary convection model for heat transfer by means of geothermal fluids in post eruptive systems, Geothermics 16 (1) (1987) 77–89.

[33] B. M. Ziapour, H. Shaker, Heat transfer characteristics of a two-phase closed thermosyphon using different working fluids, Heat and Mass Transfer/Waerme- und Stoffuebertragung 46 (3) (2010) 307–314. doi:10.1007/s00231-009-0570-1.

[34] J.-C. Ebeling, S. Kabelac, S. Luckmann, H. Kruse, Simulation and experimental validation of a 400 m vertical CO2 heat pipe for geothermal application (2016) 218–225.

[35] A. Elghool, F. Basrawi, H. Ibrahim, T. K. Ibrahim, M. Ishak, T. M. Yusof, S. A. Bagaber, Enhancing the performance of a thermo-electric generator through multi-objective optimisation of heat pipes-heat sink under natural convection, Energy Conversion and Management 209 (February) (2020) 112626. doi:10.1016/j.enconman.2020.112626.

[36] G. Fraisse, J. Ramousse, D. Sgorlon, C. Goupil, Comparison of different modeling approaches for thermoelectric elements, Energy Conversion and Management 65 (2013) 351–356. doi:10.1016/j.enconman.2012.08.022.

[37] A. Rodríguez, J. G. Vián, D. Astrain, A. Martinez, Computational model and test bench for thermoelectric power generation, for thermoelectric parameters dependent on the temperature, International Conference on Thermoelectrics, ICT, Proceedings (2006) 300–304.doi:10.1109/ICT.2006.331374.

[38] P. Aranguren, M. Araiz, D. Astrain, A. Martínez, Thermoelectric generators for waste heat harvesting: A computational and experimental approach, Energy Conversion and Management 148 (2017) 680–691. doi:10.1016/j.enconman.2017.06.040.

[39] M. Araiz, A. Martínez, D. Astrain, P. Aranguren, Experimental and computational study on thermoelectric generators using thermosyphons with phase change as heat exchangers, Energy Conversion and Management 137 (2017) 155–164. doi:10.1016/j.enconman.2017.01.046.

[40] M. Araiz, Á. Casi, L. Catalán, Á. Martínez, D. Astrain, Prospects of waste-heat recovery from a real industry using thermoelectric generators: Economic and power output analysis, Energy Conversion and Management 205 (November 2019) (2020) 112376. doi:10.1016/j.enconman.2019.112376.

[41] F. P. Brito, J. Martins, L. M. Goncalves, R. Sousa, Modelling of thermoelectric generator with heat pipe assist for range extender application, IECON Proceedings (Industrial Electronics Conference) (2011) 4589–4595.doi:10.1109/IECON.2011.6120066.

[42] F. P. Brito, A. Alves, J. M. Pires, L. B. Martins, J. Martins, J. Oliveira, J. Teixeira, L. M. Goncalves, M. J. Hall, Analysis of a Temperature-Controlled Exhaust Thermoelectric Generator During a Driving Cycle, Journal of Electronic Materials 45 (3) (2016) 1846–1870. doi:10.1007/s11664-015-4258-7.

[43] A. J. Chapman, Fundamentals of heat transfer, Macmillan Publishing Company, New York, 1987.

[44] F. P. Incropera, D. P. D. Witt, Fundamentals of heat transfer, 4th Edition, Prentice Hall.

[45] H. Forster, N. Zuber, Dynamics of Vapour Bubbles and Boiling Heat Transfer, American Institute of Chemical Engineering Journal 1 (1955) 531–535.

[46] W. Rohsenow, J. Hartnett, Y. Cho, Handbook of heat transfer, 3rd Edition, McGraw-Hill Handbooks, 1998.

[47] S. Lee, S. Song, V. Au, K. P. Moran, Constriction/spreading resistance model for electronics packaging, 4th ASME/JSME Thermal Engineering Conference 4 (1995) 199–206.
URL http://www.digikey.it/WebExport/SupplierContent/Aavid_59/PDF/Aavid_ConstrictionModel.pdf

[48] E. W. Lemmon, , I. H. Bell, M. L. Huber, M. O. McLinden, NIST Standard Reference Database 23: Reference Fluid Thermodynamic and Transport Properties-REFPROP, Version 10.0, National Institute of Standards and Technology (2018). doi:10.18434/T4JS3C.
URL https://www.nist.gov/srd/refprop

[49] L. Filippov, N. Novoselova, Vestnik Moscov, Univ. Gas. 10 (1955).

[50] W. Gambill, , Chem. Eng 66 (151) (1959).

[51] T. Graham, On the motion of gases, Phil. Trans 136 (1846) 573–631.

[52] M. M. Shah, An Improved and Extended General Correlation for Heat Transfer During Condensation, Hvac&R Research 15 (September 2009) (2009) 37–41. doi:10.1080/10789669.2009.10390871.

[53] J. L. Hoke, A. M. Clausing, T. D. Swofford, An Experimental Investigation of Convective Heat Transfer From Wire-On-Tube Heat Exchangers, Journal of Heat Transfer 119 (2) (1997) 348–356. doi:10.1115/1.2824231.

[54] M. Araiz, L. Catalan, O. Herrero, G. Perez, A. Rodriguez, Bringing Thermoelectricity into Reality, IntechOpen, 2018. doi:10.5772/intechopen.71354.
URL https://www.intechopen.com/books/bringing-thermoelectricity-into-reality/the-importance-of-the-assembly-in-thermoelectric-generators

[55] A. Rodríguez, G. Pérez-Artieda, I. Beisti, D. Astrain, A. Martínez, Influence of Temperature and Aging on the Thermal Contact Resistance in Thermoelectric Devices, Journal of Electronic Materials (2020). doi:10.1007/s11664-020-08015-y.

[56] C. Gorse, D. Johnston, M. Pritchard, A Dictionary of Construction, Surveying and Civil Engineering, Oxford University Press, 2012.

[57] II-VI Marlow, Technical Data Sheet for TG12-8.
URL https://cdn2.hubspot.net/hubfs/547732/Data_Sheets/TG12-8.pdf

[58] H. Coleman, W. Steele, Experimentation, Validation and Uncertainty. Analysis for Engineers, 3rd Edition, Wiley.

[59] Instituto Geológico Minero Español, Evaluación del potencial geotérmico superficial de Montañas de Fuego como Sistema de Roca Caliente Seca, Tech. rep. (1992).

[60] D. Gomez-Ortiz, I. Blanco-Montenegro, J. Arnoso, T. Martin-

Crespo, M. Solla, F. G. Montesinos, E. Vélez, N. Sánchez, Imaging thermal anomalies in hot dry rock geothermal systems from near-surface geophysical modelling, Remote Sensing 11 (6) (2019). doi:10.3390/rs11060675.

[61] L. Catalan, M. Araiz, P. Aranguren, D. Astrain, Design of a passive geothermal thermoelectric generator for shallow hot dry rock fields: application to Timanfaya National Park, in: XI National and II International Engineering Thermodynamics Congress. ISBN: 978-84-09-11635-5., 2019, pp. 1360–1370.

[62] Instituto para la Diversificación y Ahorro de Energía (IDAE), Guía técnica. Condiciones climáticas exteriores de proyecto., 2010.
URL http://www.idae.es/uploads/documentos/documentos_12_Guia_tecnica_condiciones_climaticas_exteriores_de_proyecto_e4e5b769.pdf

[63] Meteoblue, Clima lanzarote.
URL https://www.meteoblue.com/es/tiempo/historyclimate/climatemodelled/lanzarote_espana_2515699